

1     **Deep learning model of somatic hypermutation reveals importance of sequence context**  
2                                   **beyond targeting of AID and Pol $\eta$  hotspots**

3

4

5     **Authors and Affiliations**

6     Catherine Tang<sup>†,1</sup>, Artem Krantsevich<sup>†,1</sup>, and Thomas MacCarthy<sup>1,2,\*</sup>

7

8     <sup>†</sup> These authors contributed equally to this work

9     <sup>1</sup>Department of Applied Mathematics and Statistics, Stony Brook University, Stony Brook, NY,  
10    11794, USA

11    <sup>2</sup>Laufer Center for Physical and Quantitative Biology, Stony Brook University, Stony Brook,  
12    NY, 11794, USA

13    \*Correspondence: [thomas.maccarthy@stonybrook.edu](mailto:thomas.maccarthy@stonybrook.edu)

14

15

16    **Summary**

17

18 B-cells undergo somatic hypermutation (SHM) of the Immunoglobulin (Ig) variable region  
19 to generate high-affinity antibodies. SHM relies on the activity of activation-induced deaminase  
20 (AID), which mutates C>U preferentially targeting WRC (W=A/T, R=A/G) hotspots. Downstream  
21 mutations at WA Polymerase  $\eta$  hotspots contribute further mutations. Computational models of  
22 SHM can describe the probability of mutations essential for vaccine responses. Previous studies  
23 using short subsequences ( $k$ -mers) failed to explain divergent mutability for the same  $k$ -mer. We  
24 developed the DeepSHM (Deep learning on SHM) model using  $k$ -mers of size 5-21, improving  
25 accuracy over previous models. Interpretation of DeepSHM identified an extended DWRCT  
26 (D=A/G/T) motif with particularly high mutability. Increased mutability was further associated  
27 with lower surrounding G content. Our model also discovered a conserved AGYCTGGGGG  
28 (Y=C/T) motif within FW1 of IGHV3 family genes with unusually high T>G substitution rates.  
29 Thus, a wider sequence context increases predictive power and identifies novel features that drive  
30 mutational targeting.

31

32

### 33 **Introduction**

34

35 Upon encountering antigen, germinal center (GC) B cells undergo several programmed  
36 mutational events in secondary lymphoid organs to mount an effective humoral immune response.  
37 Somatic hypermutation (SHM) takes place in the GC dark zone whereby mostly point mutations  
38 are introduced into the Immunoglobulin (Ig) variable (V) region. Selection for mutations leading

39 to higher binding B cell receptors to cognate antigen occurs in the GC light zone, thus, producing  
40 a diverse repertoire of high-affinity antibodies (Methot and Di Noia, 2017; Pilzecker and Jacobs,  
41 2019; Rajewsky, 1996). The mutagenic enzyme, activation-induced deaminase (AID), initiates  
42 SHM (Muramatsu et al., 2000) by converting cytosine (C) to uracil (U) in single-stranded DNA  
43 (ssDNA), resulting in a U:G (guanine) mismatch (Bransteitter et al., 2003). AID displays  
44 preferential targeting at WRC/GYW "hotspot" motifs (where W=A/T, R=A/G, Y=C/T, and the  
45 underlined base indicates the mutated base in the top and bottom strand, respectively), whereas  
46 SYC/GRS "coldspots" (S=C/G) are significantly less targeted (Pham et al., 2003; Rogozin and  
47 Diaz, 2004; Rogozin and Kolchanov, 1992; Yu et al., 2004). If left unrecognized, U mismatches  
48 will act as a template T and be replicated over (Pilzecker and Jacobs, 2019). The resulting C>T  
49 transition mutation is commonly referred to as the DNA "footprint" of AID (Liu et al., 2008).  
50 Downstream DNA repair further contributes to antibody diversity that is mediated by low-fidelity  
51 polymerases. During non-canonical base-excision repair (ncBER), the U:G mismatch is  
52 recognized and excised by uracil-DNA glycosylase (UNG), resulting in an abasic site (Rada et al.,  
53 2004). Repair of these abasic sites by REV1 can cause both transition and transversion mutations  
54 at C:G base-pairs (Jansen et al., 2006). In the case of non-canonical mismatch repair (ncMMR),  
55 the U:G mismatch is recognized by the MSH2/MSH6 heterodimer. Next, EXO1 exonuclease is  
56 recruited to create a patch of ssDNA, which then allows error-prone polymerases, particularly  
57 Polymerase eta (Pol $\eta$ ), to resynthesize. Pol $\eta$  is known to create mutations at neighboring adenine  
58 (A) and thymine (T) sites of the initial AID-induced lesion, most notably at WA/TW hotspot motifs  
59 (Matsuda et al., 2001; Mayorov et al., 2005).

60 Several computational models have been developed for the SHM process and intrinsic  
61 biases exhibited by key proteins such as AID and Pol $\eta$ . These models have mainly utilized *k*-mer

62 subsequences, where  $k$  is a specified integer length, ranging between 3- to 7-mers (Cui et al., 2016;  
63 Elhanati et al., 2015; Shapiro et al., 1999; Shapiro et al., 2002; Yaari et al., 2013). Two of these  
64 models (Cui et al., 2016; Yaari et al., 2013) are widely used and have leveraged 5-mer motifs to  
65 capture the dependency of the local surrounding sequence for the middle nucleotide to mutate,  
66 while simultaneously bypassing any influence of selection. The first of these targeting models  
67 ("S5F") evaluates all possible 5-mers and synonymous (silent) mutations derived from functionally  
68 rearranged, or productive, VDJ coding sequences (Yaari et al., 2013). The second model  
69 ("RS5NF") similarly assesses 5-mers but uses both synonymous and non-synonymous  
70 (replacement) mutations from non-productively (non-functional) rearranged sequences (Cui et al.,  
71 2016). Such models have been used to simulate B cell repertoire lineages by constructing a set of  
72 hypothetical sequences that have been mutated in a sequential manner as governed by, for example,  
73 the underlying S5F substitution scores (Krantsevich et al., 2021; Sheng et al., 2017). Although  $k$ -  
74 mer approaches are generally able to capture some key local intrinsic biases of SHM, such as  
75 hotspot targeting, there is evidence that shorter  $k$ -mers are insufficient to properly characterize  
76 differential SHM targeting. For example, a recent study extended a local sequence (5-mer) context  
77 model and improved accuracy by including parameters describing the position within the IGHV  
78 gene (Spisak et al., 2020). Another study compared the mutability of identical 5-mer (middle  
79 position +/-2nt) motifs at different positions within an IGHV gene (Zhou and Kleinstein, 2020),  
80 and found that the mutation frequency of these motif-allele pairs (MAPs) positively correlates with  
81 the overall mutability of a wider neighborhood of motifs, suggesting that an extended  $k$ -mer may  
82 better capture SHM.

83 Earlier studies have shown that using deep learning is effective in different genomic  
84 applications; for example, convolutional neural networks (CNNs) in extracting conserved

85 sequence motifs among target sequences (Alipanahi et al., 2015; Kelley et al., 2016; Zhou and  
86 Troyanskaya, 2015). In this study, we adopted a deep learning approach using a 2-D CNN to  
87 analyze extended *k*-mer lengths to better understand the underlying SHM process. We demonstrate  
88 that our model, DeepSHM (Deep learning on SHM), can more accurately represent the SHM  
89 process by evaluating longer *k*-mers of up to 21 nts. Additionally, DeepSHM using 15-mers as  
90 inputs was able to recapitulate AID WRC/GYW hotspot motifs and identify an extended DWRCT  
91 motif. Neural network predictions are notoriously difficult to explain (the "black box" problem),  
92 but many new methods are available to interpret results (Koo and Ploenzke, 2020). We used one  
93 such method to identify a negative association between increased mutability at a site and its  
94 surrounding G content. On the other hand, lower mutation frequency was correlated with increased  
95 substitution rates of certain substitution types, particularly for G>T and C>A mutations.  
96 Furthermore, many highly conserved sites within G-rich sub-regions belonging to several IGHV3  
97 genes display an extremely high bias towards creating G mutations, some of which may participate  
98 in the formation of G-quadruplex (G4) structures.

99

100

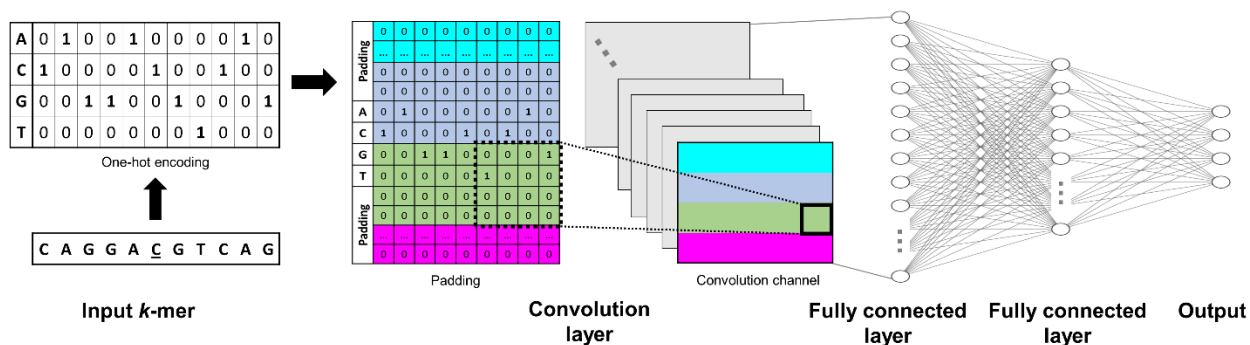
## 101 **Results**

102

### 103 **Deep learning can more accurately represent SHM mutabilities and substitution biases**

104

105 The objective of our analysis was to use supervised deep learning to build an accurate  
 106 convolutional neural network (CNN) for SHM and, as much as possible, identify novel features  
 107 contributing to mutability. We chose CNNs because we still expected mutation frequency to  
 108 depend on recurring motifs that might occur at any position in the sequence (most obviously, AID  
 109 hotspots), a task CNNs are well suited to. The workflow of our network consists of an input layer  
 110 that processes a  $k$ -mer subsequence represented in its one-hot encoding format (i.e. a  $4 \times k$  matrix  
 111 of zeros and ones), followed by a convolution layer and two fully connected layers as the hidden  
 112 layers, and finally the output layer of size  $4 \times 1$  or  $1 \times 1$ , depending on the task that is being predicted  
 113 (**Figure 1**, see Methods). Several hyperparameters, including dropout rate and learning rate, were  
 114 fine-tuned with our model as well (**Supplementary Table 1**). We defined a model that would  
 115 separate mutations on each strand (which are predominantly at C and A on the top strand and at G  
 116 and T on the bottom strand) at the input level. To achieve this, we identified a simple solution  
 117 using padding that assigns a row in each channel of the convolution layer output separately to each  
 118 strand (**Figure 1**). CNNs are also often used together with attribution methods such as Integrated  
 119 Gradients, to help with interpretation of the results.

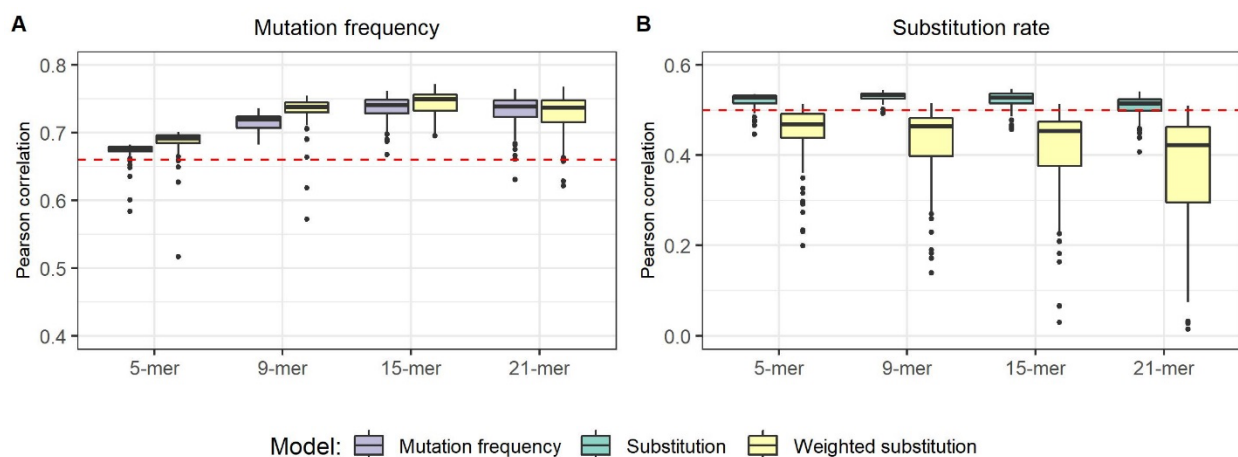


120  
 121 **Figure 1. DeepSHM model architecture.** Each model had an input layer, one convolution layer, two fully connected  
 122 layers, and an output layer. The input layer was a  $4 \times k$  dimensional one-hot encoded matrix ( $k$  is length of

123 subsequence). The dimension of the output layer was dependent on the task: substitution ( $4 \times 1$ ), mutation frequency  
124 ( $1 \times 1$ ), or weighted substitution ( $4 \times 1$ ). For the convolutional layer, ‘same’ padding was used to allow the model to  
125 process top and bottom strand mutations separately. With ‘same’ padding, the output of each convolutional channel  
126 has the same shape as the input ( $4 \times k$ ) with the following properties: the first and the fourth rows are populated with  
127 zeros only (there was no real input, only padding; cyan and magenta rows); the input used for the second (light blue)  
128 row contained two rows of padding and two data rows corresponding to A or C nucleotides only; and similarly, the  
129 input used for the third (green) row also contained two rows of padding and two rows of data corresponding to G or  
130 T nucleotides. Since AID and Pol $\eta$  target C and A sites respectively, this approach was taken with the expectation of  
131 helping the model distinguish top and bottom strands.

132 As a starting point, we trained two CNN models, which we collectively refer to as  
133 DeepSHM (Deep learning on SHM), to separately predict mutation frequency and substitution  
134 rates, calculated from previously published B cell repertoire data containing non-productively  
135 rearranged and clonally independent VDJ coding sequences (Tang et al., 2020), for varying  $k$ -mer  
136 lengths (see Methods). We trained both models independently using different combinations of  $k$ -  
137 mer lengths and hyperparameters as listed in **Supplementary Table 1**. We found that for  
138 predicting mutation frequency, 15-mers were moderately better than 9-mers (purple boxplots in  
139 **Figure 2A**, Mann-Whitney U test:  $P < 2.2 \times 10^{-16}$ ) and that further extending the motif length to 21  
140 did not improve accuracy since both produced an overall maximum correlation (across  
141 hyperparameters) of 0.76 (**Figure 2A, Table 1**). Thus, using  $k$ -mers of length 15 or longer  
142 outperformed shorter lengths, specifically 5-mers and 9-mers (**Table 1**), suggesting that an  
143 extended DNA motif can better model the SHM process. However, using longer  $k$ -mers did not  
144 substantially improve the model that predicts SHM substitution bias alone, achieving an average  
145 correlation of 0.55 for 15-mers (green boxplots in **Figure 2B, Table 1**), but which is similar for  
146 different lengths. For the interpretability analysis below, we chose to use the best 15-mer models  
147 to keep the  $k$ -mer length consistent for comparisons across all models. In order to check if the

148 performance of the models leading to the best results was consistent, we also trained 30 different  
149 iterations of each model, keeping the hyperparameters fixed but using different random seeds. We  
150 found the standard deviation across correlations was very small, at 0.002 for the mutation  
151 frequency model and 0.001 for the substitution rate model, showing the strong consistency of our  
152 results.



153  
154 **Figure 2. Performance of DeepSHM.** Boxplots describing the distribution (across random hyperparameters) of  
155 Pearson correlations between DeepSHM predictions and empirical data (y-axis) are shown for different input *k*-mers  
156 (x-axis) for (A) mutation frequencies, and (B) substitution rates, for all three models (mutation frequency, substitution,  
157 and weighted substitution). Red dashed lines signify correlations of predicted S5F values, which uses 5-mers.

158 We next sought to compare DeepSHM against the widely used S5F model that is based on  
159 5-mer motifs (Yaari et al., 2013). To ensure a fair comparison, we generated an S5F targeting  
160 model using the same data set that was used to train DeepSHM, as well as the same cross-validation  
161 scheme (see Methods). Using the same test set splits as above, we found that there was an average  
162 correlation of 0.66 between the predicted S5F model mutabilities and empirical mutation  
163 frequency, and an average correlation of 0.50 for predicted S5F substitution scores and empirical  
164 substitution rates (red dashed lines in **Figure 2**, **Table 1**). The substitution model slightly (but



165 statistically significantly) outperformed S5F for all  $k$ -mer values we analyzed. The mutation  
 166 frequency model achieved a modest improvement over S5F using 5-mers as an input, and this  
 167 difference became more evident for 9-, 15-, and 21-mers (**Figure 2A, Table 1**). We also similarly  
 168 computed 30 iterations (using different random seeds) of the best 15-mer models for both mutation  
 169 frequency and substitution models, and found these iterations to have significantly greater  
 170 accuracy than S5F both individually and in aggregate ( $P < 1.8 \times 10^{-6}$  for each model, Wilcoxon  
 171 signed-rank test). Overall, these results show that our deep learning approach successfully extracts  
 172 meaningful information from the wider sequence context to improve predictions.

Model	Test set	S5F (5-mer)	DeepSHM (5-mer)	DeepSHM (9-mer)	DeepSHM (15-mer)	DeepSHM (21-mer)
Substitution rate	IGHV1	0.52	0.57	0.57	0.58	0.57
	IGHV3	0.49	0.52	0.52	0.53	0.52
	IGHV4	0.48	0.53	0.53	0.54	0.52
	IGHV2, 5, 6, 7	0.52	0.52	0.54	0.54	0.53
	<b>Avg correlation</b>	<b>0.50</b>	<b>0.54</b>	<b>0.54</b>	<b>0.55</b>	<b>0.54</b>
	Best - S5F	NA	0.04	0.04	0.05	0.04
	Mean - S5F	NA	0.02	0.03	0.02	0.01
P-value	NA	1.18E-13	1.28E-17	2.04E-13	2.25E-04	
Mutation frequency	IGHV1	0.69	0.72	0.78	0.8	0.81
	IGHV3	0.65	0.69	0.72	0.74	0.73
	IGHV4	0.64	0.69	0.73	0.78	0.78
	IGHV2, 5, 6, 7	0.66	0.64	0.68	0.73	0.74
	<b>Avg correlation</b>	<b>0.66</b>	<b>0.68</b>	<b>0.73</b>	<b>0.76</b>	<b>0.76</b>

	Best - S5F	NA	0.02	0.08	0.1	0.1
	Mean - S5F	NA	0.01	0.06	0.08	0.07
	P-value	NA	6.41E-14	1.28E-17	1.28E-17	1.28E-17
Weighted substitution (substitution rate)	IGHV1	0.52	0.55	0.55	0.53	0.53
	IGHV3	0.49	0.5	0.5	0.5	0.49
	IGHV4	0.48	0.49	0.51	0.48	0.5
	IGHV2, 5, 6, 7	0.52	0.49	0.52	0.49	0.51
	<b>Avg correlation</b>	<b>0.50</b>	<b>0.51</b>	<b>0.52</b>	<b>0.50</b>	<b>0.51</b>
	Best - S5F	NA	0.04	0.09	0.11	0.11
	Mean - S5F	NA	0.03	0.07	0.08	0.07
	P-value	NA	7.51E-16	9.47E-17	1.28E-17	2.33E-17
Weighted substitution (mutation frequency)	IGHV1	0.69	0.77	0.81	0.84	0.84
	IGHV3	0.65	0.69	0.72	0.73	0.71
	IGHV4	0.64	0.68	0.7	0.74	0.73
	IGHV2, 5, 6, 7	0.66	0.66	0.74	0.77	0.77
	<b>Avg correlation</b>	<b>0.66</b>	<b>0.70</b>	<b>0.74</b>	<b>0.77</b>	<b>0.76</b>
	Best - S5F	NA	0.01	0.02	0.01	0.01
	Mean - S5F	NA	-0.05	-0.07	-0.09	-0.14
	P-value	NA	2.06E-15	1.53E-16	3.19E-17	1.28E-17

173 **Table 1. Cross-validation of various input *k*-mer sequences.** The correlations of repeatedly trained models using  
174 different random seeds (but the same hyperparameters) for neural network training had small standard deviations, in  
175 all cases below 0.01. P-values are from a Wilcoxon signed-rank test comparing the training results for each model  
176 with the corresponding S5F model accuracy. P-values were corrected (Benjamini-Hochberg) for multiple  
177 comparisons.

178           To identify associations between mutation frequency and specific substitutions, we further  
179 constructed a DeepSHM model to predict the "weighted substitution" of a  $k$ -mer, i.e., the product  
180 of the percentage of each observable substitution type (e.g G>N) and the mutation frequency of  
181 the  $k$ -mer (see Methods). Note that this weighted substitution metric is a vector representing the  
182 four ordered DNA bases, with a "0" placed at the position that matches the middle nucleotide of  
183 the  $k$ -mer. Since weighted substitution constitutes aspects of both the observable mutation  
184 frequency and substitution rate of the middle nucleotide of a given  $k$ -mer, we were able to evaluate  
185 DeepSHM on each metric separately. Although this model made poorer substitution rate  
186 predictions on average (varying hyperparameters) than S5F (**Table 1**), the best model performed  
187 similarly to S5F for substitution rates while, surprisingly, performing slightly better than any  
188 model in predicting mutation frequency. Cross-validation in this instance produced a range of  
189 average correlations between 0.50-0.52 for predicted substitution rates – a level similar to that of  
190 S5F (**Figure 2B, Table 1**). On the other hand, DeepSHM of weighted substitution values was  
191 marginally better at predicting mutation frequency for 15-mers (correlation: 0.77) than the  
192 previous standalone model that was tasked to learn mutation frequency only as well as being better  
193 than S5F. (**Figure 2A, Table 1**). Since the weighted substitution model was able to perform at a  
194 level slightly better to the standalone mutation frequency model for longer  $k$ -mers and substantially  
195 better for shorter (5-mer, 9-mer), this suggested a possible association between the projected  
196 substitution bias of a site and overall mutability and furthermore, that interpretability methods  
197 might uncover these (see below).

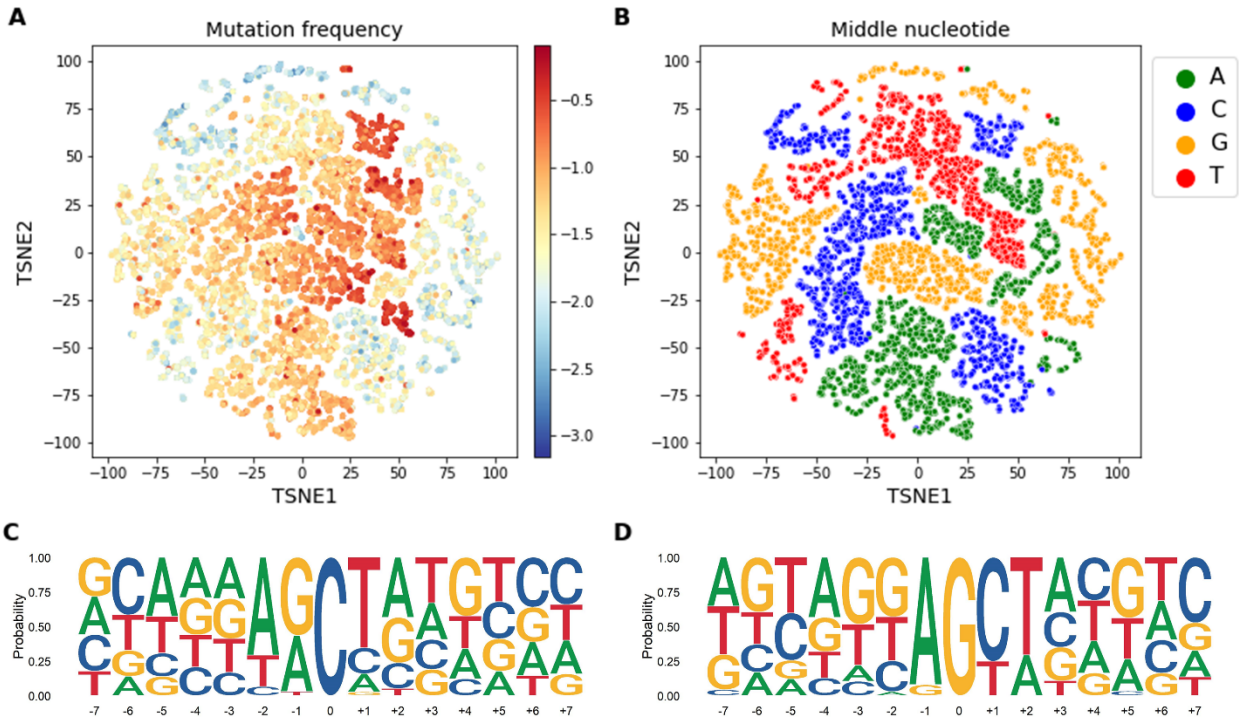
198

199 **Interpretation of the DeepSHM network reveals extended hotspot motifs**

200

201           A complication often associated with deep neural networks is model interpretability (the  
202 “black box” problem). One way we interrogated the predictions made by DeepSHM, and what it  
203 has learned about the SHM process, was to analyze the output of the penultimate layer of each 15-  
204 mer based model. In particular, analyzing the output, or “encodings”, of this layer can be viewed  
205 as an alternative, and more informative, way of representing the input 15-mer. To visualize the  
206 multi-dimensional encodings of the individual 15-mers, we used t-SNE, a dimensionality reduction  
207 technique, to project each onto a 2-dimensional embedding (see Methods). At this point in order  
208 to make full use of the data, we merged all of the 15-mer data into one training set, and then trained  
209 three new individual models (one for each output type) using the hyperparameters which  
210 previously led to the best cross-validation results. The analyses we present below are derived from  
211 the DeepSHM models that were trained using this merged data set.

212           We began by identifying features learned by DeepSHM that predicted weighted  
213 substitutions. Since weighted substitution is a measure of both mutation frequency and substitution  
214 bias, the embedding should capture both metrics simultaneously. Each point in the resulting t-SNE  
215 embedding in **Figure 3A** represents a single 15-mer and is colored according to its corresponding  
216 mutation frequency. We identified several clusters of 15-mers that are mostly grouped by similar  
217 mutation rates, including those expressing high mutability. Clusters with mid to high mutation  
218 frequencies are similarly within close proximity but displayed no obvious groupings other than  
219 being mostly located towards the center. When we considered the middle nucleotide of each 15-  
220 mer, we observed that these clusters also shared the same middle nucleotide (**Figure 3B**),  
221 suggesting that the network identified as a key feature the “0” value in the weighted substitution  
222 output vector that is associated with the middle nucleotide.

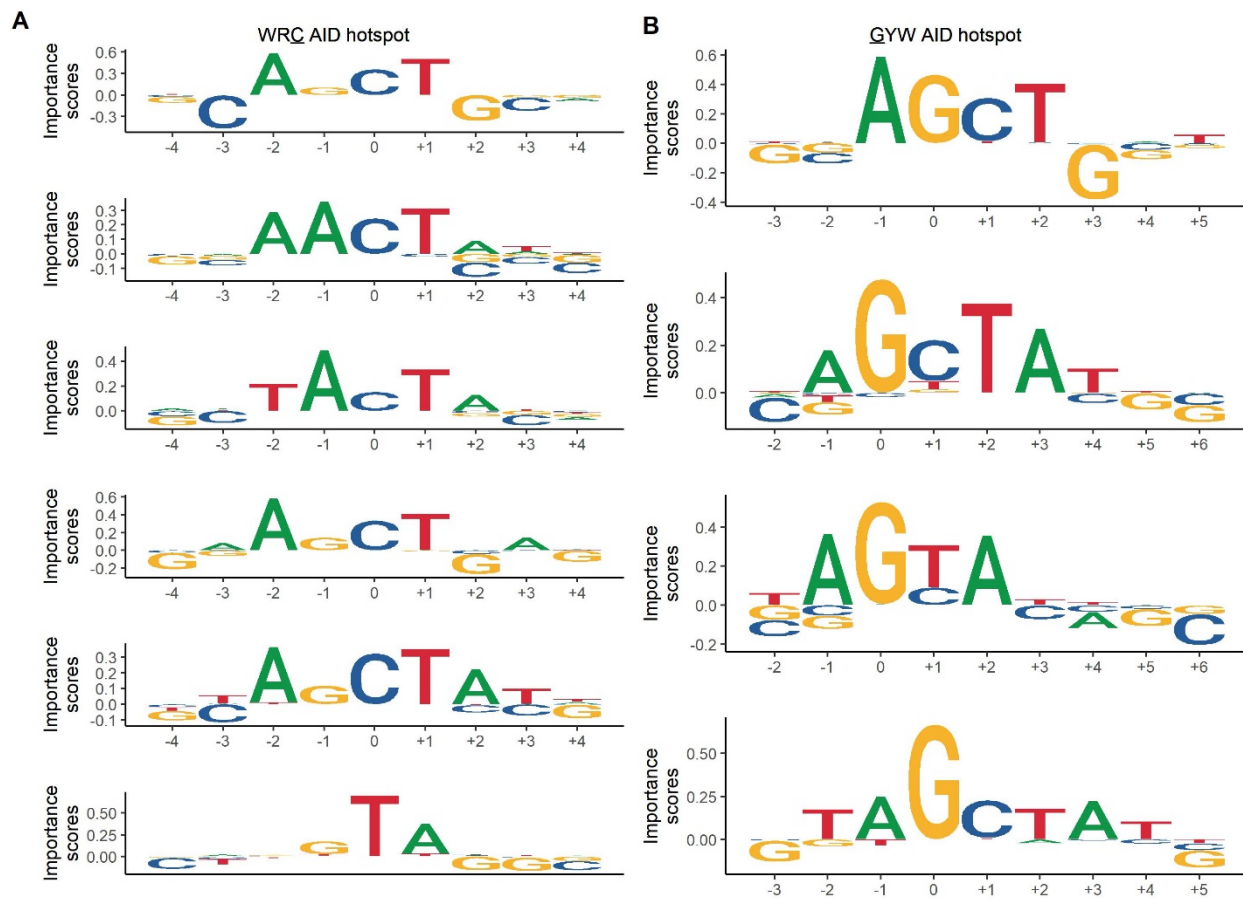


223

224 **Figure 3. Neural network encodings analysis: weighted substitution model.** Each point in the t-SNE embedding  
225 represents a single 15-mer processed through the truncated model (to extract the output of the penultimate layer)  
226 originally trained to learn the associated weighted substitutions (see Methods) and is colored according to its  
227 corresponding (A) mutation frequency (log<sub>10</sub>), and (B) middle nucleotide. Consensus sequences derived from the  
228 highest mutated cluster identified using k-means clustering on the embedding of 15-mers containing either (C) a  
229 middle C nucleotide or (D) a G nucleotide (clusters 10 and 16 in Supplementary Table 2).

230 Next, we applied k-means clustering on the embedding as a way to isolate cluster  
231 boundaries (Supplementary Figure 1, see Methods). We subsequently created a sequence logo  
232 plots representing each cluster shown in Supplementary Table 2. As expected, clusters with the  
233 highest mutation frequencies had inner subsequences containing AID (C cluster 10, G cluster 16)  
234 and Polη (A clusters 1 and 2, T cluster 20) hotspots. For AID, these are WRC (Figure 3C) and  
235 GYW motifs (Figure 3D). Within the two most highly targeted AID hotspot clusters there is a  
236 substantial presence of both WGC/GCW and WAC/GTW contexts, rather than only the well-

237 known WGCW overlapping hotspot motif (Tang et al., 2020; Wei et al., 2015). Furthermore, even  
238 when we include WAC/GTW, there is a preference for a T base at the 3' end of the WRC hotspot,  
239 and conversely, an even stronger bias for an A base at the 5' end of the GYW hotspot (**Figure 3C,**  
240 **D**). This motif is consistent with a genome-wide study of AID mutations in mice that reported  
241 observing high mutability at AACT and AGCT motifs in both strands (Álvarez-Prado Á et al.,  
242 2018). When we assessed the mutability of all possible WRCN (N=A/C/G/T) motifs separately,  
243 we observed WRCT to be the most highly mutated in each case (**Supplementary Figure 2**).  
244 Previous studies identified WRCY/RGYW (Y=C/T, R=A/G) and later WRCH/DGYW  
245 (H=A/C//T, D=A/G/T) to be a better predictor of mutability at C:G bases (Rogozin and Diaz, 2004;  
246 Rogozin and Kolchanov, 1992). However, we discovered some inconsistencies with these  
247 definitions, as AGCC was found to be the least mutated of the AGCN motifs and WRCG was not  
248 always the least mutated, on both strands. Overall, these early hotspot definitions may have been  
249 too broad, and WRCT/AGYW is a more consistent predictor of AID targeting. Lastly, we also  
250 noted that among the least mutated *k*-mer clusters, many were G-rich in their surrounding context  
251 (for example, C clusters 8 and 9, A cluster 4, T cluster 21), and particularly for G (G clusters 12  
252 and 14) (**Supplementary Table 2**).



253

254 **Figure 4. Recurrent motifs identified by TF-MoDISco.** TF-MoDISco results using the Integrated Gradients as base-  
255 level importance scores of 15-mers whose middle nucleotide conformed to a (A) WRC or (B) GYW AID hotspot  
256 motif.

257 As a complementary way to find sequence motifs associated with mutability, we used TF-  
258 MoDISco (Transcription Factor Motif DIScovery), a program for identifying recurring motif  
259 patterns in genomic data (see Methods) (Shrikumar et al., 2018). We applied TF-MoDISco to the  
260 standalone model that predicts only mutation frequency because we reasoned that sequence  
261 features related to mutability would be more easily identifiable since the model is only required to  
262 learn a single task. TF-MoDISco uses importance scores, which can be derived from many  
263 machine learning methods, to produce a set of unique motifs learned by the model (see Methods).

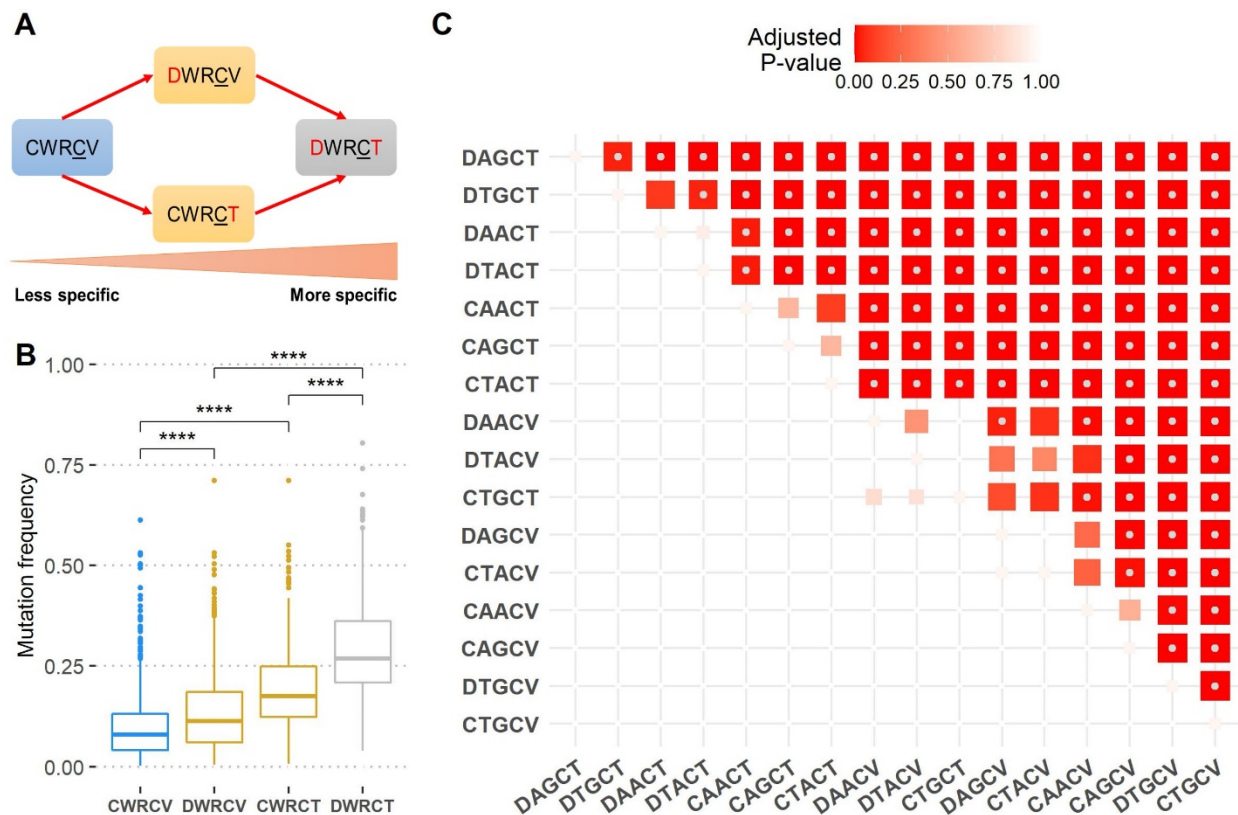
264 We began by analyzing the importance scores derived from Integrated Gradients (Sundararajan et  
265 al., 2017) of 15-mers whose middle nucleotide conformed a WRC/GYW AID hotspot motif. As  
266 expected, the positively contributing sites in the set of ensuing motifs aligned with the hotspot  
267 motifs (**Figure 4A, B**). In addition, TF-MoDISco again revealed a preference for having a T base  
268 at the +1 position of the WRC (WRCT, **Figure 4A**) and an A base at the -1 position of the GYW  
269 (AGYW, **Figure 4B**).

270 In addition to WRCT/AGYW being a well-represented motif identified by TF-MoDISco,  
271 as measured by having positive contributions to mutability (above horizontal axis on **Figure 4A**),  
272 we also noticed many neighboring C and G bases contained negative contributions (below  
273 horizontal axis on **Figure 4A**), most evidently at the C located at the -3 position of the WRC  
274 hotspot, and the G located at the +3 position of the GYW hotspot (**Figure 4B**). Here, the negative  
275 contribution at the -3 position signifies that having a C at that position reduces mutational targeting  
276 to the middle C. By the same token, a mutation that changes the -3 position from C will increase  
277 the likelihood of the middle C subsequently being targeted. This observation supports our recently  
278 published study where we observed a strong positive “mutual association” – a correlation metric  
279 describing the impact of mutating one site and its effect at another site – between CC (or GG) pairs  
280 distanced by two nucleotides (Krantsevich et al., 2021). In that study we were able to explain most  
281 of such correlations in terms of overlapping AID and/or Polη hotspots, with the CNNC/GNNG  
282 motif being one the exceptions which we suggested might be explained by AID processivity (Pham  
283 et al., 2003; Storb et al., 2009). However, the TF-MoDISco analysis suggests a different  
284 explanation in which the absence of a C in the -3 position might be a part of an extended AID  
285 hotspot, defining CWRC as being similar to a sequential overlap motif, which we previously  
286 defined (Krantsevich et al., 2021) as a motif in which an initial mutation creates a new hotspot that



287 previously did not exist. Here, although the WRC hotspot did previously exist, a mutation in the  
288 first C would create a DWRC (D=A/G/T) motif, potentially with higher mutability.

289 We next sought to determine whether adding the 5' D or 3' T context of the canonical WRC  
290 hotspot is more influential in terms of increasing its susceptibility to AID mutagenesis. To address  
291 this, we increased the hotspot specificity step by step, starting from CWRCV (V=A/C/G) and  
292 assessed the impact a single change in the motif at either the first C or V site, causing a DWRCV  
293 or CWRCT intermediate hotspot to form respectively, has on mutability (**Figure 5A**). We found  
294 that both DWRCV and CWRCT intermediate hotspots were shown to mutate significantly more  
295 than CWRCV (**Figure 5B**). We also discovered that the mutability of the DWRC hotspot, which  
296 contains the extended hotspot in both 5' and 3' directions, was significantly higher than both  
297 intermediate hotspots (**Figure 5B**). Performing a pairwise comparison between the mutation  
298 frequency of all 16 individual (D/C)WRC(T/V) contexts further confirmed that those containing  
299 both a 5' D and 3' T were significantly more mutated than the remaining hotspot motifs, with  
300 DAGCT being the most mutated (**Figure 5C, Supplementary Table 3**). Additionally, the next  
301 three successively mutated hotspots followed a CWRCT context, overall suggesting the 3' T to be  
302 more impactful to AID recognition than the 5' D, but the addition of both substantially increases  
303 targeting in human V regions.



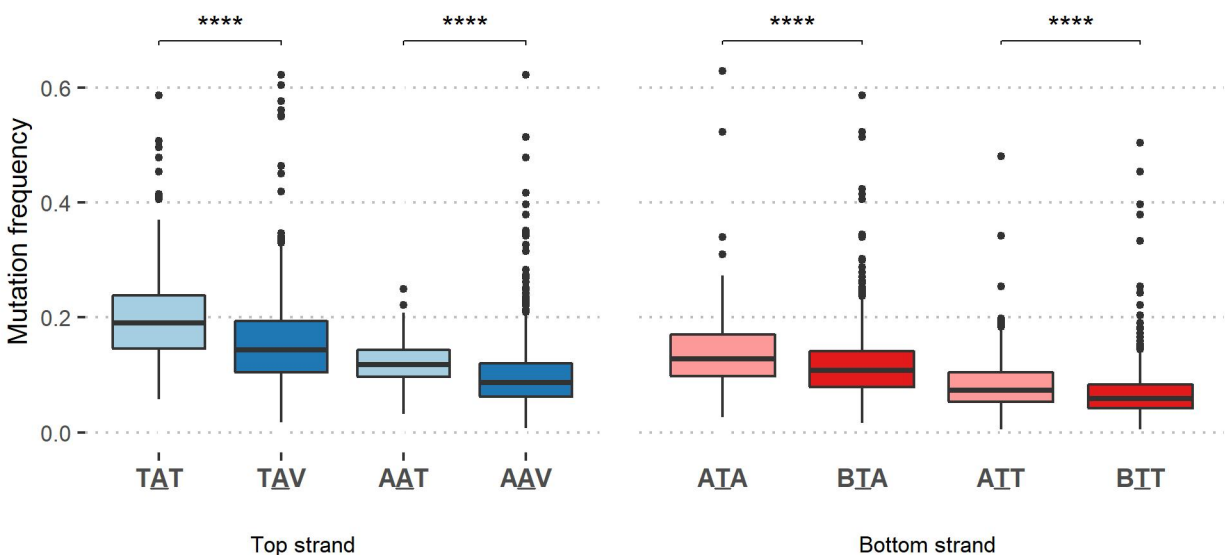
304

305 **Figure 5. Mutability of extended AID hotspots.** (A) Schematic showing an increase of AID hotspot specificity (left  
 306 to right). (B) Boxplots displaying the mutability of different (C/D)WRC(T/V) hotspot contexts, where D=A/G/T,  
 307 V=A/C/G. Asterisks indicate significance ( $p \leq 0.0001$ ) of a one-sided Mann-Whitney U test comparing the greater  
 308 mutation frequency of the boxplot on the right against the one on the left. (C) Pairwise comparison of mutability for  
 309 all 16 (C/D)WRC(T/V) hotspot contexts. Boxes represent the p-value - adjusted for multiple comparisons (Benjamini-  
 310 Hochberg correction) - of a one-sided Mann-Whitney U test comparing the greater mutation frequency of the hotspot  
 311 indicated by the row to the left, against the hotspot shown in the column below. Rows and columns are ordered by  
 312 mean mutation frequency (high to low). The color and size of each box is scaled according to the adjusted p-value.  
 313 Gray dots inside boxes indicate p-values  $\leq 0.05$ .

314 In addition, another secondary motif that unexpectedly emerged from the TF-MoDISco  
 315 analysis of WRC/GYW 15-mers did not contain a positively contributing C nucleotide; rather it  
 316 conformed to a TA Pol $\eta$  hotspot (Figure 4A, bottom). Having a TA hotspot appear while

317 specifically analyzing only 15-mers containing WRC hotspots reveals the importance of attracting  
318 Pol $\eta$  to these areas. This finding is consistent with our previous analysis highlighting the  
319 importance of co-localization of AGCT overlapping AID hotspots and Pol $\eta$  hotspots within the  
320 CDRs (Tang et al., 2020; Wei et al., 2015).

321 The TA motif also emerged when we applied TF-MoDISco to all 15-mers conforming to  
322 either a WA (Supplementary Figure 3A) or TW Pol $\eta$  hotspot (Supplementary Figure 3B). In  
323 addition to our model identifying both the TA and AA hotspot motifs as important, it also identified  
324 a TAT/ATA motif as a special case for both strands. Further analysis showed that WAT/ATW  
325 hotspots mutate significantly more than their WAV/BTW counterparts (Figure 6). Thus, while TA  
326 hotspots consistently have higher mutability than AA, the presence of a 3' T individually increases  
327 the mutability of each of these Pol $\eta$  hotspots.



328  
329 **Figure 6. Mutability of extended Pol $\eta$  hotspot motifs.** Boxplots comparing the mutation frequency of various top  
330 strand WAT against WAV (blue), and bottom strand ATW against BTW (red) motifs. Asterisks indicate significance

331 ( $p \leq 0.0001$ ) of a one-sided Mann-Whitney U test comparing the greater mutation frequency of the boxplot on the left  
332 against the one on the right.

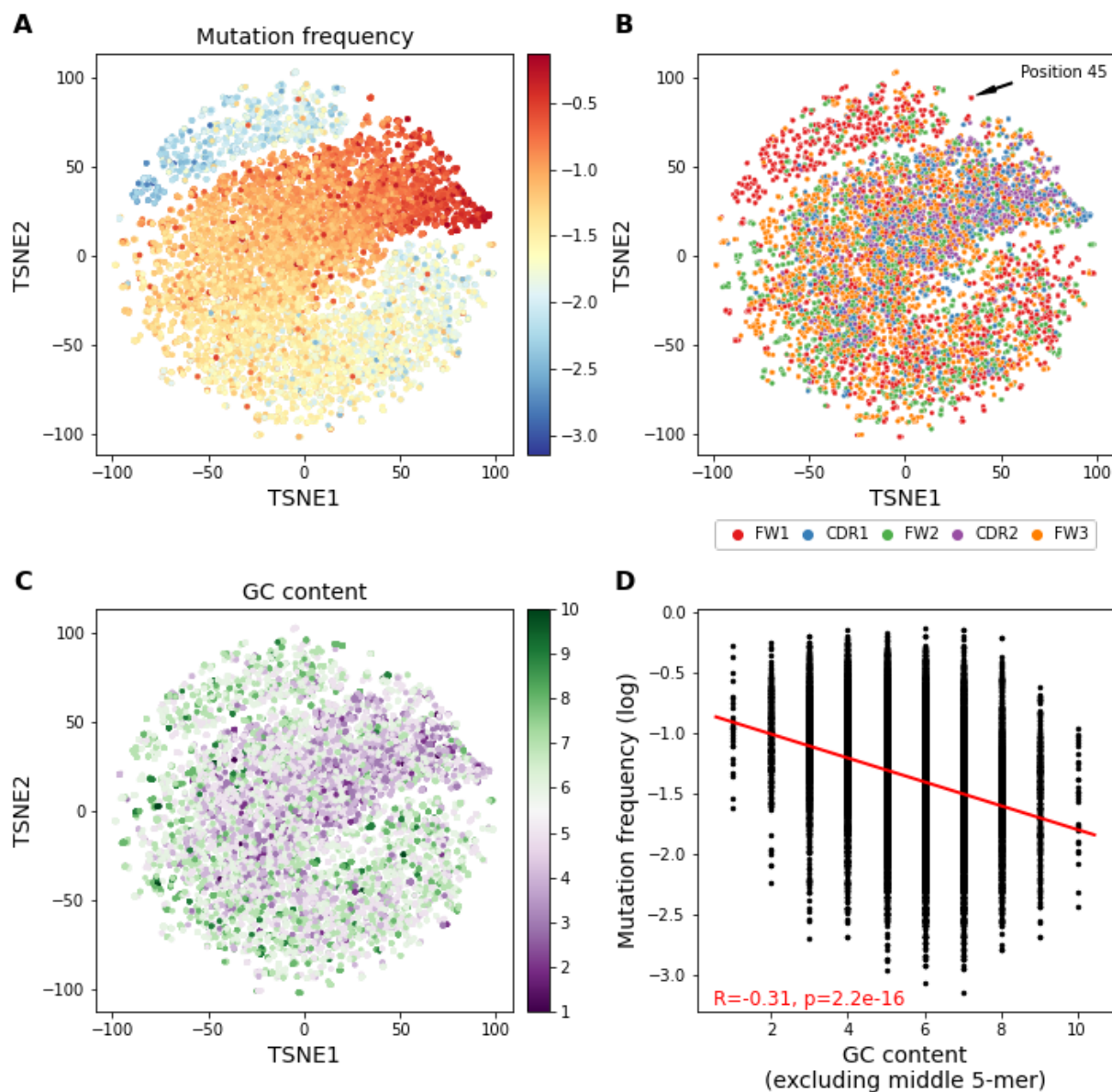
333

### 334 **Highly targeted sites display a lower surrounding GC content**

335

336 We next applied the same t-SNE methodology to the DeepSHM model that predicted only  
337 mutation frequency. We found that the organization of the subsequent embedding followed a  
338 direction of descending mutation frequency, with the highest mutating 15-mers located at the mid-  
339 to upper-right portion of the plot (**Figure 7A**). A cluster of low-mutating 15-mers was also isolated  
340 in the upper-left (**Figure 7A**), which was enriched with ~76% of FW1 15-mers (**Figure 7B**).  
341 Additionally, we examined the possible influence of the local surrounding sequence by calculating  
342 the individual base content of the four DNA bases in each 15-mer. However, the inner 5-mer,  
343 which contains the dominant context, was excluded when computing all base counts. When we  
344 colored the t-SNE embedding according to the GC content of each 15-mer, we observed that GC  
345 content increases along the same direction as decreasing mutability seen previously (**Figure 7C**).  
346 Quantifying this observation more formally, we indeed found a significant negative correlation  
347 between the GC content and the mutation frequency of the 15-mers ( $R=-0.31$ ,  $P<2.2 \times 10^{-16}$ ; **Figure**  
348 **7D**). On the other hand, when we considered each individual base count independently, we  
349 observed that the count of G nucleotides specifically shows a stronger negative correlation ( $R=-$   
350  $0.19$ ) than the C nucleotide count ( $R=-0.084$ ) alone (**Supplementary Figure 4A**), although both  
351 correlations are highly significant ( $P<2.2 \times 10^{-16}$ ). This result is consistent with the cluster analysis  
352 above (**Supplementary Table 2**) where we observed several clusters with G-rich  $k$ -mers and low

353 mutation frequencies. If we further separate the mutation frequencies into categories defined by  
354 the middle nucleotide, we find that G content has a consistent negative correlation regardless  
355 (column G of **Supplementary Figure 4B**). More generally, A and T richness (columns A and T  
356 of **Supplementary Figure 4B**) shows a consistent positive or sometimes non-significant  
357 correlation, whereas C and G richness shows a consistent negative (or non-significant) correlation.  
358 In summary, it appears that low-mutating sites generally have a high local GC (and particularly G)  
359 content, and conversely, that highly targeted sites display an elevated local AT (particularly A)  
360 content.



361

362 **Figure 7. Neural network encodings analysis: mutation frequency model.** Each point in the t-SNE embedding

363 represents a single 15-mer processed through the truncated model (to extract the output of the penultimate layer)

364 trained on mutation frequencies (see Methods) and is colored according to its corresponding (A) mutation frequency

365 ( $\log_{10}$ ), and (B) by Ig V sub-region location as defined by IMGT. (C) The t-SNE embedding is colored according to

366 the GC content of each 15-mer. The calculated GC content excludes the middle 5-mer context of the 15-mer to remove

367 any confounding AID hotspot or coldspot bias. (D) Computed Pearson correlation between mutation frequency and

368 GC content, again excluding the middle 5-mer.

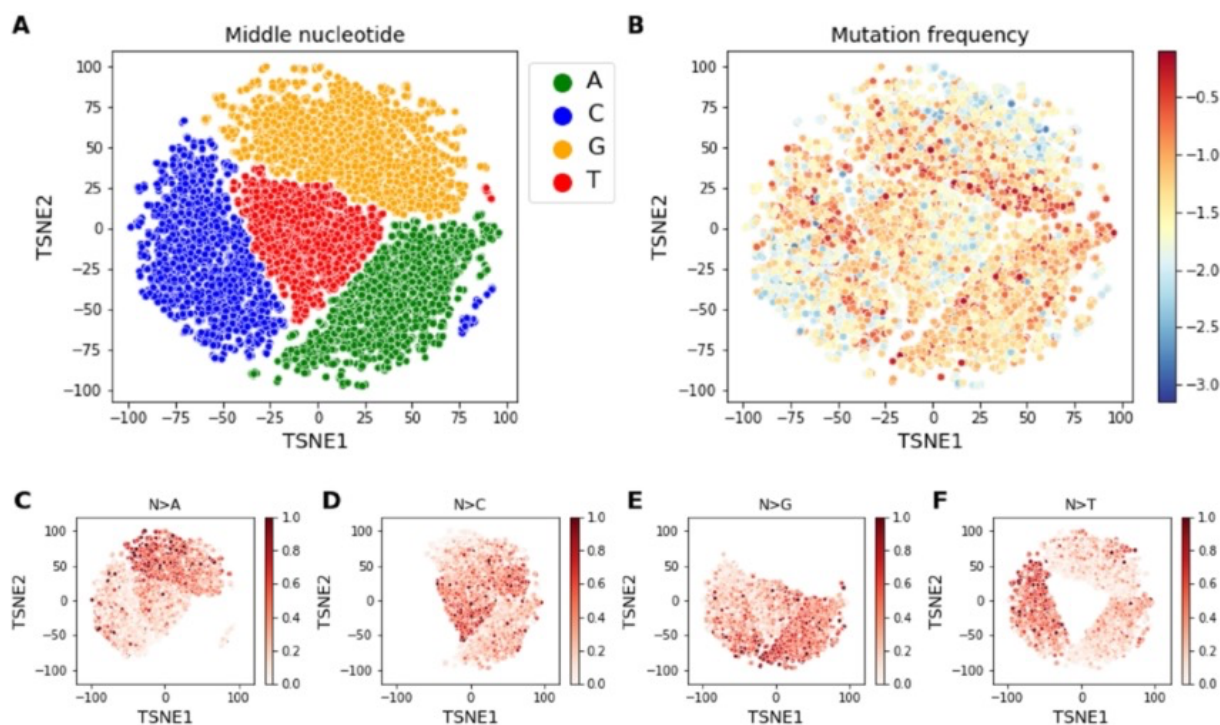
369

370 **Conserved FW1 sites surrounded by clusters of AID coldspots in IGHV3 genes display a**  
371 **high T>G transversion bias**

372

373 We now analyzed the standalone model predicting only substitution rates to gain possible  
374 insight into additional substitution biases exhibited by AID or downstream error-prone DNA  
375 damage response pathways, for example, as a result of REV1 or Pol $\eta$  intervention during non-  
376 canonical base-excision repair (BER) and non-canonical mismatch repair (MMR), respectively.  
377 The resulting t-SNE embedding from this model identified four main clusters, as well as two much  
378 smaller satellite clusters, with each cluster containing 15-mers that share a common middle  
379 nucleotide (**Figure 8A**). A distinction between 15-mers with high and low mutation frequencies  
380 could also be observed based on their location on opposite ends of the cluster, especially for  
381 clusters containing either a C or G middle nucleotide, with high-mutating 15-mers typically located  
382 on the side closest to the center (**Figure 8B**). Since the model was tasked with learning the  
383 distributed substitution rates of each 15-mer, we next sought to evaluate the embedding by the rate  
384 of each individual substitution type (e.g. C>T). In certain clusters, a similar gradient of high to low  
385 substitution rates could also be seen as we observed for mutation frequency (**Figure 8C-F**). For  
386 instance, we noticed the rate of G>T substitutions increasing from the side nearest to the origin  
387 towards the outer boundaries of the cluster (top-right cluster in **Figure 8F**), which was associated  
388 with a shift towards decreasing mutation frequencies in the same cluster while proceeding in the  
389 same direction (**Figure 8B**). To evaluate this trend more closely, we analyzed three human IGHV  
390 genes from different families for which we had the most data (IGHV1-18, IGHV3-23, IGHV4-

391 34), so as to include sites with low mutation frequencies at high coverage, and calculated the  
392 correlation between mutation frequency and rate of substitution for each substitution type. As an  
393 example, for IGHV3-23 we found the most significant negative correlations to be at C>A  
394 mutations ( $R=-0.33$ ,  $p=0.0058$ ), and the reverse, G>T ( $R=-0.24$ ,  $p=0.022$ ; **Supplementary Figure**  
395 **5**). Alternatively, we observed a significant positive correlation between mutation frequency and  
396 C>T transition mutations ( $R=0.29$ ,  $p=0.018$ ; **Supplementary Figure 5**). Similar patterns were also  
397 observed for IGHV1-18\*01 and IGHV4-34\*01 (**Supplementary Figure 5**). These results are  
398 consistent with replication bypass (predominantly causing C>T) being favored over BER at sites  
399 with high mutation frequency.



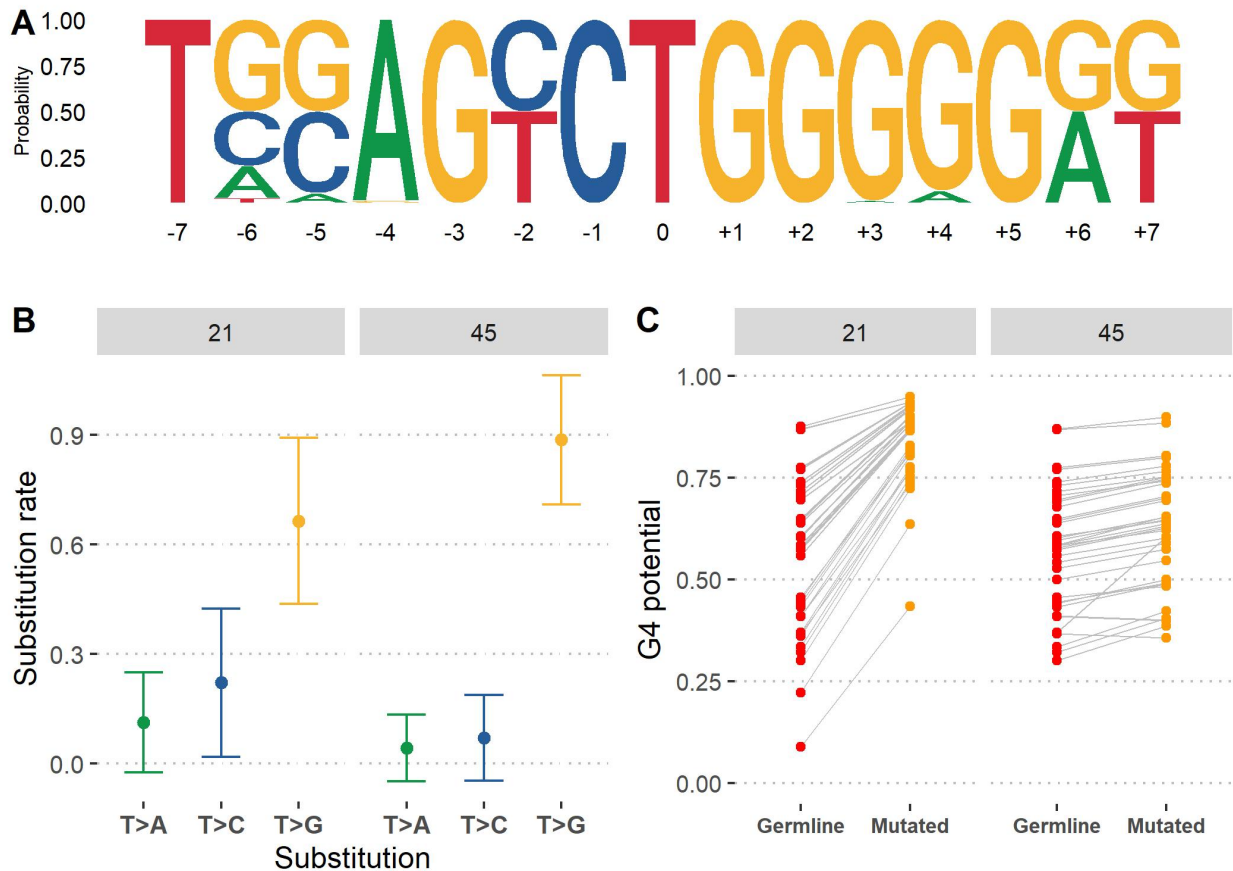
400  
401 **Figure 8. Neural network encodings analysis: substitution model.** Each point in the t-SNE embedding represents  
402 a single 15-mer processed through the truncated model (to extract the output of the penultimate layer) trained to learn  
403 the associated substitution rates (see Methods) and is colored according to its corresponding (A) middle nucleotide,



404 and **(B)** mutation frequency ( $\log_{10}$ ). **(C-F)** The t-SNE embedding is colored by the rate of substitution for the middle  
405 nucleotide of every 15-mer to mutate to A (N>A); to C (N>C); to G (N>G); and to T (N>T), respectively.

406 In the t-SNE analysis of the substitution model, we also discovered two small clusters of  
407 15-mers containing a C and T as their middle nucleotide (**Figure 8A**) that did not group with their  
408 respective larger clusters, suggesting that these particular sites might have distinct substitution  
409 patterns. Generating the consensus sequence of the outlier T cluster revealed a partially conserved  
410 AGYCTGGGGG sequence (**Figure 9A**). When we examined these subsequences more closely,  
411 we discovered that they were located only in IGHV3 family genes at either position 21 or position  
412 45 according to the IMGT unique numbering system (Lefranc, 2001) (**Supplementary Figure 6**).  
413 The motif was also surprisingly common. At position 21 it appeared in 37 different alleles (across  
414 19 genes) and was fully conserved in all alleles. Coincidentally, the motif also appeared in 37  
415 different alleles (across 18 genes) at position 45, although it differed slightly at the +3 and +4  
416 positions (**Figure 9A**). These two sets of alleles only partially overlap, such that 15 alleles had the  
417 motif at both positions 21 and 45. Thus, this specific motif in FW1 of the IGHV3 family genes  
418 appears to be highly conserved evolutionarily, suggesting a possible functional role. The rates of  
419 substitution at these sites were also found to be highly biased towards creating T>G mutations,  
420 with an average T>G rate of about 0.66 at position 21, and an even greater rate of 0.89 at position  
421 45 (background rate:  $0.28 \pm 0.23$ ) (**Figure 9B, Table 2**). A previous study using Sanger sequencing  
422 data that was limited to IGHV3-23 and the pseudogene IGHV3-h had noted similarly high T>G  
423 substitution rates at positions 21 (for IGHV3-h) and 45 (for IGHV3-23) (Ohm-Laursen and  
424 Barington, 2007). Although the T subjected to mutation at both positions did not conform to a  
425 bottom strand TW Pol $\eta$  hotspot, these genes at position 45 displayed a relatively high average  
426 mutation frequency of  $0.17 \pm 0.08$  (**Table 2**), which is somewhat unusual given that mutations are

427 generally more biased towards the CDRs than FW regions (Cohen et al., 2011; Shapiro et al.,  
 428 2002), and that we reported above that many sites within FW1 tended to display low mutability  
 429 (Figure 7A, B).



430

431 **Figure 9. Evaluation of the T outlier cluster in the DeepSHM substitution model.** (A) Sequence logo  
 432 representation of the 15-mers appearing in the T outlier cluster in Figure 8A (right-hand side, red dots). (B)  
 433 Substitution rates of T>A, T>C, and T>G for 15-mers corresponding to 37 IGHV3 alleles separately at IMGT positions  
 434 21 and 45. Bars represent  $\pm 1$  standard deviation. (C) G-quadruplex (G4) formation potential for the same IGHV3  
 435 alleles in (B). G4 potentials (y-axis) are computed using the germline IGHV sequence ("Germline") and the mutated  
 436 sequence ("Mutated") containing a single simulated T>G mutation at either IMGT positions 21 or 45.

437 While examining the C outlier cluster (Figure 8A), we found the consensus sequence to  
 438 be more diverse compared to the outlier with a middle T (Supplementary Figure 7A). The

439 sequence variation seen here was partly due to the fact that the 15-mers that constituted this cluster  
440 belonged to many other IGHV families besides IGHV3 and across different sub-regions of the IgV  
441 (**Supplementary Figure 6**). On the other hand, we noticed some overlap between both outlier  
442 clusters since, in some cases, the C corresponded to positions 20 and 44 that preceded the middle  
443 T of the other outlier cluster (**Supplementary Figure 7A, Table 2**). We further found these sites  
444 to have a similar elevated C>G substitution rate (mean rate of 0.62 compared to background mean  
445 of 0.33,  $P < 2.2 \times 10^{-16}$ ) (**Supplementary Figure 7B, Table 2**), suggesting the model distinguished  
446 sites with a general preference to create G mutations.

447         Given that the sites with strikingly high T>G and C>G substitution rates we identified here  
448 are in adjoining G-rich sub-regions (**Figure 9A, Supplementary Figure 7A**), we evaluated the  
449 possible influence these mutations might have on the formation of G-quadruplex (G4) structures.  
450 In a recent study, we assessed the potential for DNA G4 structures to form in the IgV region, using  
451 a pre-trained deep learning model that computes the G4 potential of a linear DNA sequence (Tang  
452 and MacCarthy, 2021). There we found that the IGHV3 family had the highest propensity to form  
453 stable G4s in the top strand. We now sought to assess the overall mutational effect on G4 assembly  
454 of the IGHV3 sites that are biased towards G. Following the methodology of our previous study,  
455 we calculated the difference between the predicted G4 potential of the germline with that of the  
456 sequence with a single mutation at either position 21 or 45. Here, we found that a T>G mutation  
457 at position 21 elevated average G4 potentials to a very high value of  $0.84 \pm 0.10$  compared to a  
458 germline value (already relatively high) of  $0.54 \pm 0.19$ , whereas the same mutation occurring at  
459 position 45 displayed a far smaller average increase of  $0.05 \pm 0.04$  (**Figure 9C, Table 2**). As for  
460 the remaining cases, there seemed to be little effect of C>G mutations on G4 potential (**Table 2**).

461 Interestingly, we made another observation regarding the instances where an A nucleotide disrupts  
 462 the run of G

IMGT position	15-mer middle nucleotide	n	Avg. substitution rate to G	Avg. mutation frequency	Avg. germline G4 potential	Avg. mutated G4 potential	Avg. difference in G4 potential (mutated - germline)
1	C	1	0.67	0.02	0.01	0.01	0.00
20	C	31	0.50 ± 0.32	0.01 ± 0.01	0.54 ± 0.20	0.64 ± 0.19	0.09 ± 0.02
21	T	37	0.66 ± 0.23	0.05 ± 0.03	0.54 ± 0.19	0.84 ± 0.10	0.29 ± 0.10
34	C	19	0.60 ± 0.37	0.03 ± 0.05	0.07 ± 0.08	0.07 ± 0.08	0.01 ± 0.00
44	C	38	0.77 ± 0.24	0.02 ± 0.01	0.56 ± 0.17	0.64 ± 0.18	0.07 ± 0.04
45	T	37	0.89 ± 0.18	0.17 ± 0.08	0.58 ± 0.15	0.63 ± 0.14	0.05 ± 0.04
48	A	1	0.79	0.11	0.37	0.56	0.19
49	A	5	0.79 ± 0.12	0.07 ± 0.03	0.37 ± 0.07	0.53 ± 0.05	0.16 ± 0.02
61	C	45	0.67 ± 0.14	0.04 ± 0.02	0.54 ± 0.19	0.54 ± 0.19	0.01 ± 0.01
101	C	1	0.52	0.11	0.01	0.01	0.00
167	C	1	0.46	0.52	0.37	0.41	0.04
173	C	3	0.64 ± 0.29	0.09 ± 0.09	0.04 ± 0.02	0.04 ± 0.02	0.00 ± 0.00
180	C	1	0.20	0.03	0.01	0.01	0.00
214	C	4	0.51 ± 0.26	0.13 ± 0.06	0.08 ± 0.06	0.10 ± 0.07	0.01 ± 0.01
249	C	15	0.59 ± 0.24	0.06 ± 0.02	0.08 ± 0.09	0.08 ± 0.09	0.00 ± 0.01
268	C	44	0.55 ± 0.19	0.06 ± 0.03	0.55 ± 0.18	0.53 ± 0.18	-0.01 ± 0.01

463 **Table 2. Summary statistics on outlier C and T clusters from Figure 8A.**

464 nucleotides at the +3 or +4 positions (**Figure 9A**) which was that these sites also displayed  
 465 high A>G substitution rates ( $0.79 \pm 0.11$ ; **Table 2**, positions 48 and 49). This hypothetical mutation

466 also caused a moderate, though substantial, increase in G4 potential ( $0.17 \pm 0.02$ , **Table 2**). These  
467 findings reveal that particular recurring mutations in this sub-region may promote G4 formation,  
468 and that the bias towards generating new G sites suggests specific DNA repair enzymes may be  
469 recruited to these sub-regions within FW1.

470

471

## 472 **Discussion**

473

474 In this study, we leveraged deep learning to gain novel insights into SHM, a key process  
475 in antibody affinity maturation. We trained multiple deep learning models using a convolutional  
476 neural network (CNN) framework to analyze DNA *k*-mer subsequences of various lengths, ranging  
477 from 5 to 21 nts, derived from human IGHV germline sequences. Using a high-quality data set  
478 containing non-productive B cell repertoire data, the model was tasked to learn two focal aspects  
479 of SHM: the frequency of mutation at a given site, and the spectrum of mutations that can arise at  
480 this site (substitution). Understanding the propensity of a site to mutate and the underlying  
481 substitution biases that ensue can lead to a better understanding of how AID is recruited to and  
482 targets the Ig V region, as well as the associated downstream DNA repair mechanisms that follow  
483 AID deamination.

484 We began by developing three models, collectively referred to as DeepSHM, to predict  
485 separate tasks for a given *k*-mer: observable mutation frequency; distributed substitution rates; and  
486 a combination of both measures (weighted substitution). We found that predicting substitution

487 rates did not substantially depend on the  $k$ -mer size, while 15-mers were optimal for predicting  
488 mutation frequencies (**Figure 2, Table 1**). Additionally, DeepSHM predicted both substitution  
489 rates and mutation frequencies more accurately than the widely used S5F targeting model for all  
490  $k$ -mer sizes we evaluated ( $k = 5, 9, 15$  and  $21$ ) (**Table 1**). Even though we were able to outperform  
491 S5F in representing substitution biases, the correlation between our predictions and empirical data  
492 was moderate ( $\sim 0.55$ ), suggesting that the processes underlying SHM substitution biases may be  
493 more fundamentally random than mutational site targeting alone. Error-prone DNA repair  
494 processes downstream of AID are highly complex. For example, while Pol $\eta$  is biased towards  
495 making  $W\bar{A}>W\bar{G}$  mutations (Zhang et al., 2014) and plays a dominant role in generating mutations  
496 at A:T sites, many A:T mutations still occur in its absence (Saribasak et al., 2009) that are mediated  
497 by other polymerases (Maul et al., 2016). Similarly complex, BER is biased towards transversions  
498 but can also repair faithfully, with a further dependence on hotspot mutability (Pérez-Durán et al.,  
499 2012). Thus, downstream repair processes may simply be too complex, or genuinely random, to  
500 be captured well by a model that depends on sequence context alone.

501 In order to uncover some of the hidden features learned by DeepSHM, we analyzed the  
502 output, or encodings, obtained from the penultimate layer of the network predicting weighted  
503 substitution using input 15-mers, and performed t-SNE, a method of dimensionality reduction, to  
504 visualize the encodings in two dimensions. The subsequent embedding formed clusters of 15-mers  
505 that were distinguished by mutation frequency and middle nucleotide (**Figure 3A, B**). Individual  
506 clusters containing a C or G middle nucleotide that were associated with high mutability, assumed  
507 to be relevant to AID hotspots, revealed a strong preference for a T base at the +1 position of the  
508 top strand AID  $WRC\bar{C}$  ( $W=A/T, R=A/G$ ) hotspot, including for  $WAC\bar{C}$  motifs that are not part of a  
509  $WGC\bar{W}$  motif, and similarly, an A base at the -1 position of the bottom strand  $\bar{G}YW$  ( $Y=C/T$ )

510 context (**Figure 3C, D**). As an alternative way to identify sequence features, we applied TF-  
511 MoDISco (see Methods) to reveal recurrent genomic patterns using importance scores extracted  
512 from the model for each 15-mer. This approach confirmed the importance of the T base at the +1  
513 position of WRC (**Figure 4A**) and the A base at the -1 position of the bottom strand GYW hotspot  
514 (**Figure 4B**). An early study by Rogozin and Diaz reported the WRCH/DGYW (H=A/C/T,  
515 D=A/G/T) to be a good predictor of mutability at C:G bases (Rogozin and Diaz, 2004), but we  
516 found WRCT to be a more consistent definition. The authors of the S5F model also supported the  
517 WRCH definition since they found their model can capture the higher mutability rate seen at  
518 certain WRCA motifs (Yaari et al., 2013), presumably at the AGCA overlapping hotspot.  
519 However, previous hotspot definitions have largely failed to describe targeting beyond the -2  
520 position of the WRC motif. We further identified having a C at the -3 position of WRC or a G at  
521 the +3 position of GYW as a strong negative contribution, i.e., as a reduced effect on targeting.  
522 Thus, our results suggest the typical AID hotspot definition might be extended to DWRCT  
523 (D=A/G/T). Comparing the mutation frequencies of the individual DWRCT hotspot motifs  
524 showed the 3' T to be more important for AID recognition than the 5' D alone, however, together  
525 they have a synergistic effect that makes mutability between 1.8-fold (for TAC) and 4.7-fold (for  
526 TGC) higher (**Figure 5C, Supplementary Table 3**).

527 We next applied the same t-SNE methodology on the two developed standalone models  
528 that separately predicted either the mutation frequency or substitution rates of the 15-mer middle  
529 nucleotides. The t-SNE embedding on the independent DeepSHM model predicting only mutation  
530 frequency revealed a significant negative correlation between the mutability of a site and the  
531 surrounding GC content of the 15-mer (**Figure 7D**). This finding alternatively suggests that highly  
532 mutated sites may have evolved to have a richer local AT content. This *in vivo* result is consistent

533 with earlier *in vitro* results that considered AID targeting on artificial substrates (Abdouni et al.,  
534 2018).

535 On the other hand, the t-SNE embedding stemming from the standalone substitution model  
536 hinted at plausible associations, both positive and negative, between mutation frequency and  
537 certain transition and transversion mutations (**Figure 8B-F**). We next analyzed multiple genes  
538 representing different IGHV families containing the largest amounts of mutation data in order to  
539 avoid any potential sites with few observable mutations, such as coldspots. We observed a negative  
540 correlation between mutability and substitution rates specifically for C>A and G>T transversion  
541 mutations (**Figure 8, Supplementary Figure 6**) and, on the other hand, positive correlations for  
542 C>T and G>A transitions (**Supplementary Figure 6**). The trend for increased transition mutations  
543 at highly mutating AID hotspots mediated by UNG2 had previously been observed in experiments  
544 using 3T3 (mouse fibroblast) cells (Pérez-Durán et al., 2012), although the particular bias against  
545 C:G>A:T transversions was not apparent. Previous work has also shown that UNG2 is cell-cycle  
546 regulated, possibly mediated by FAM72A (Feng et al., 2020), and active primarily during G1  
547 (Sharbeen et al., 2012). Although AID is also primarily active during G1, it may sometimes persist  
548 for slightly longer than UNG2 and thus highly targeted sites may avoid BER especially when the  
549 mutations occur just before the cell enters S phase, which would lead to fixation of C>T transitions  
550 via replication bypass. Alternative polymerases may also be preferentially recruited to some sites.  
551 For example, in DT40 (chicken) B-cell lines, the POLD3 subunit of Polymerase delta (Pol $\delta$ ) has  
552 been proposed as a specific mechanism for both C>A and G>T mutations (Hirota et al., 2015;  
553 Pilzecker and Jacobs, 2019).

554 Additionally, we investigated two outlier clusters from the substitution model embedding  
555 that contained 15-mers having a C and T middle nucleotide that did not group with their respective



556 larger clusters (**Figure 8A**). A closer analysis revealed that the T outlier contained a highly  
557 conserved AGYCTGGGGG consensus sequence that was derived from two independent sites  
558 located in FW1 from multiple IGHV3 alleles (**Figure 9A, Table 2**). Both outlier clusters also  
559 displayed significantly elevated T>G (**Figure 9B, Table 2**) and C>G substitution rates  
560 (**Supplementary Figure 7, Table 2**) respectively. In our recent study on G-quadruplexes (G4s)  
561 in IGHV genes, we observed the IGHV3 family to form G4s more favorably on the top strand, as  
562 measured by their predicted G4 potential using a pre-trained CNN model (Tang and MacCarthy,  
563 2021). Given the strong preference for creating G mutations in these FW1 sub-regions, we  
564 evaluated the impact of these mutations on G4 potential. In some cases, the resulting G mutation  
565 led to a strong increase in G4 potential, particularly at position 21 (**Figure 9C, Table 2**), whereas  
566 for other sites, the effect was mostly negligible (**Table 2**). Notably however, a high A>G  
567 substitution rate was also observed at the +3 or +4 positions (**Figure 9A**), which were also  
568 associated with increase in G4 potential (**Table 2**). These biased A>G mutations may further be  
569 related to previous work that found that a repeated mutation that occurs in one IGHV allele often  
570 matches the sequence variant of a different allele (Saini and Hershberg, 2015). Alternatively, these  
571 mutations may be related to R-loop initiation, which forms in G-rich non-template DNA, possibly  
572 forming in FW1 of these IGHV3 genes. Studies have found that reducing G-density in mammalian  
573 Ig Switch regions compromises class-switch recombination efficiency and R-loops from forming  
574 (Roy et al., 2008; Zhang et al., 2014). The high rate of T>G and C>G transversions also suggests  
575 that particular repair enzymes may be recruited to these sub-regions during SHM.

576

577 **Limitations of the study**

578

579 In principle, a wider range of k-mers, as well as a greater variety of neural network architectures,  
580 might have been considered for this study. However, since the tuning of each model takes a  
581 substantial amount of computational resources and time, we considered a reduced number of  
582 models. Additionally, we limited this study to consider data only for human, the species for  
583 which we had high quality (UMI barcoded) data in high abundance, although the approach could  
584 be extended to other species such as mouse in future work.

585

## 586 **Acknowledgements**

587 We would like to extend our gratitude to Sergio Roa Gómez for his comments and suggestions.

588

## 589 **Author contributions**

590 C.T., A.K., and T.M. conceived the idea, analyzed the results, and wrote the manuscript. C.T. and  
591 A.K. developed the model and performed computational analysis. All authors contributed to the  
592 article and approved the submitted version.

593

## 594 **Declaration of interests**

595 The authors declare no competing interests.

## References

- 596  
597  
598 Abdouni, H.S., King, J.J., Ghorbani, A., Fifield, H., Berghuis, L., and Larijani, M. (2018).  
599 DNA/RNA hybrid substrates modulate the catalytic activity of purified AID. *Molecular*  
600 *Immunology* *93*, 94-106.
- 601 Alipanahi, B., Delong, A., Weirauch, M.T., and Frey, B.J. (2015). Predicting the sequence  
602 specificities of DNA- and RNA-binding proteins by deep learning. *Nat Biotechnol* *33*, 831-838.
- 603 Álvarez-Prado Á, F., Pérez-Durán, P., Pérez-García, A., Benguria, A., Torroja, C., de Yébenes,  
604 V.G., and Ramiro, A.R. (2018). A broad atlas of somatic hypermutation allows prediction of  
605 activation-induced deaminase targets. *J Exp Med* *215*, 761-771.
- 606 Bransteitter, R., Pham, P., Scharff, M.D., and Goodman, M.F. (2003). Activation-induced cytidine  
607 deaminase deaminates deoxycytidine on single-stranded DNA but requires the action of RNase.  
608 *Proc Natl Acad Sci U S A* *100*, 4102-4107.
- 609 Cohen, R.M., Kleinstein, S.H., and Louzoun, Y. (2011). Somatic hypermutation targeting is  
610 influenced by location within the immunoglobulin V region. *Mol Immunol* *48*, 1477-1483.
- 611 Cui, A., Di Niro, R., Vander Heiden, J.A., Briggs, A.W., Adams, K., Gilbert, T., O'Connor, K.C.,  
612 Vigneault, F., Shlomchik, M.J., and Kleinstein, S.H. (2016). A Model of Somatic Hypermutation  
613 Targeting in Mice Based on High-Throughput Ig Sequencing Data. *J Immunol* *197*, 3566-3574.
- 614 Elhanati, Y., Sethna, Z., Marcou, Q., Callan, C.G., Jr., Mora, T., and Walczak, A.M. (2015).  
615 Inferring processes underlying B-cell repertoire diversity. *Philos Trans R Soc Lond B Biol Sci*  
616 *370*.
- 617 Feng, Y., Li, C., Stewart, J., Barbulescu, P., Desivo, N.S., Álvarez-Quilón, A., Pezo, R.C., Perera,  
618 M.L.W., Chan, K., Tong, A.H.Y., *et al.* (2020). FAM72A antagonizes UNG2 to promote  
619 mutagenic uracil repair during antibody maturation. *bioRxiv*, 2020.2012.2023.423975.
- 620 Hirota, K., Yoshikiyo, K., Guilbaud, G., Tsurimoto, T., Murai, J., Tsuda, M., Phillips, L.G., Narita,  
621 T., Nishihara, K., Kobayashi, K., *et al.* (2015). The POLD3 subunit of DNA polymerase  $\delta$  can  
622 promote translesion synthesis independently of DNA polymerase  $\zeta$ . *Nucleic acids research* *43*,  
623 1671-1683.
- 624 Jansen, J.G., Langerak, P., Tsaalbi-Shtylik, A., van den Berk, P., Jacobs, H., and de Wind, N.  
625 (2006). Strand-biased defect in C/G transversions in hypermutating immunoglobulin genes in  
626 Rev1-deficient mice. *J Exp Med* *203*, 319-323.
- 627 Kelley, D.R., Snoek, J., and Rinn, J.L. (2016). Basset: learning the regulatory code of the  
628 accessible genome with deep convolutional neural networks. *Genome Res* *26*, 990-999.
- 629 Koo, P.K., and Ploenzke, M. (2020). Deep learning for inferring transcription factor binding sites.  
630 *Curr Opin Syst Biol* *19*, 16-23.

- 631 Krantsevich, A., Tang, C., and MacCarthy, T. (2021). Correlations in Somatic Hypermutation  
632 Between Sites in IGHV Genes Can Be Explained by Interactions Between AID and/or Polη  
633 Hotspots. *Frontiers in Immunology 11*.
- 634 Lefranc, M.P. (2001). IMGT, the international ImMunoGeneTics database. *Nucleic Acids Res 29*,  
635 207-209.
- 636 Liu, M., Duke, J.L., Richter, D.J., Vinuesa, C.G., Goodnow, C.C., Kleinstein, S.H., and Schatz,  
637 D.G. (2008). Two levels of protection for the B cell genome during somatic hypermutation. *Nature*  
638 *451*, 841-845.
- 639 Matsuda, T., Bebenek, K., Masutani, C., Rogozin, I.B., Hanaoka, F., and Kunkel, T.A. (2001).  
640 Error rate and specificity of human and murine DNA polymerase  $\epsilon$ . *J Mol Biol 312*, 335-346.
- 641 Maul, R.W., MacCarthy, T., Frank, E.G., Donigan, K.A., McLenigan, M.P., Yang, W., Saribasak,  
642 H., Huston, D.E., Lange, S.S., Woodgate, R., *et al.* (2016). DNA polymerase  $\iota$  functions in the  
643 generation of tandem mutations during somatic hypermutation of antibody genes. *J Exp Med 213*,  
644 1675-1683.
- 645 Mayorov, V.I., Rogozin, I.B., Adkison, L.R., and Gearhart, P.J. (2005). DNA polymerase  $\epsilon$   
646 contributes to strand bias of mutations of A versus T in immunoglobulin genes. *J Immunol 174*,  
647 7781-7786.
- 648 Methot, S.P., and Di Noia, J.M. (2017). Molecular Mechanisms of Somatic Hypermutation and  
649 Class Switch Recombination. *Adv Immunol 133*, 37-87.
- 650 Muramatsu, M., Kinoshita, K., Fagarasan, S., Yamada, S., Shinkai, Y., and Honjo, T. (2000). Class  
651 switch recombination and hypermutation require activation-induced cytidine deaminase (AID), a  
652 potential RNA editing enzyme. *Cell 102*, 553-563.
- 653 Ohm-Laursen, L., and Barington, T. (2007). Analysis of 6912 unselected somatic hypermutations  
654 in human VDJ rearrangements reveals lack of strand specificity and correlation between phase II  
655 substitution rates and distance to the nearest 3' activation-induced cytidine deaminase target. *J*  
656 *Immunol 178*, 4322-4334.
- 657 Pérez-Durán, P., Belver, L., de Yébenes, V.G., Delgado, P., Pisano, D.G., and Ramiro, A.R.  
658 (2012). UNG shapes the specificity of AID-induced somatic hypermutation. *J Exp Med 209*, 1379-  
659 1389.
- 660 Pham, P., Bransteitter, R., Petruska, J., and Goodman, M.F. (2003). Processive AID-catalysed  
661 cytosine deamination on single-stranded DNA simulates somatic hypermutation. *Nature 424*, 103-  
662 107.
- 663 Pilzecker, B., and Jacobs, H. (2019). Mutating for Good: DNA Damage Responses During Somatic  
664 Hypermutation. *Front Immunol 10*, 438.

- 665 Rada, C., Di Noia, J.M., and Neuberger, M.S. (2004). Mismatch recognition and uracil excision  
666 provide complementary paths to both Ig switching and the A/T-focused phase of somatic mutation.  
667 *Mol Cell* *16*, 163-171.
- 668 Rajewsky, K. (1996). Clonal selection and learning in the antibody system. *Nature* *381*, 751-758.
- 669 Rogozin, I.B., and Diaz, M. (2004). Cutting edge: DGYW/WRCH is a better predictor of  
670 mutability at G:C bases in Ig hypermutation than the widely accepted RGYW/WRCY motif and  
671 probably reflects a two-step activation-induced cytidine deaminase-triggered process. *J Immunol*  
672 *172*, 3382-3384.
- 673 Rogozin, I.B., and Kolchanov, N.A. (1992). Somatic hypermutagenesis in immunoglobulin genes.  
674 II. Influence of neighbouring base sequences on mutagenesis. *Biochim Biophys Acta* *1171*, 11-18.
- 675 Roy, D., Yu, K., and Lieber, M.R. (2008). Mechanism of R-loop formation at immunoglobulin  
676 class switch sequences. *Mol Cell Biol* *28*, 50-60.
- 677 Saini, J., and Hershberg, U. (2015). B cell variable genes have evolved their codon usage to focus  
678 the targeted patterns of somatic mutation on the complementarity determining regions. *Mol*  
679 *Immunol* *65*, 157-167.
- 680 Saribasak, H., Rajagopal, D., Maul, R.W., and Gearhart, P.J. (2009). Hijacked DNA repair proteins  
681 and unchained DNA polymerases. *Philos Trans R Soc Lond B Biol Sci* *364*, 605-611.
- 682 Shapiro, G.S., Aviszus, K., Ikle, D., and Wysocki, L.J. (1999). Predicting regional mutability in  
683 antibody V genes based solely on di- and trinucleotide sequence composition. *J Immunol* *163*,  
684 259-268.
- 685 Shapiro, G.S., Aviszus, K., Murphy, J., and Wysocki, L.J. (2002). Evolution of Ig DNA sequence  
686 to target specific base positions within codons for somatic hypermutation. *J Immunol* *168*, 2302-  
687 2306.
- 688 Sharbeen, G., Yee, C.W., Smith, A.L., and Jolly, C.J. (2012). Ectopic restriction of DNA repair  
689 reveals that UNG2 excises AID-induced uracils predominantly or exclusively during G1 phase. *J*  
690 *Exp Med* *209*, 965-974.
- 691 Sheng, Z., Schramm, C.A., Kong, R., Program, N.C.S., Mullikin, J.C., Mascola, J.R., Kwong,  
692 P.D., and Shapiro, L. (2017). Gene-Specific Substitution Profiles Describe the Types and  
693 Frequencies of Amino Acid Changes during Antibody Somatic Hypermutation. *Front Immunol* *8*,  
694 537.
- 695 Shrikumar, A., Tian, K., Shcherbina, A., Avsec, Z., Banerjee, A., Sharmin, M., Nair, S., and  
696 Kundaje, A. (2018). Technical Note on Transcription Factor Motif Discovery from Importance  
697 Scores (TF-MoDISco). *bioRxiv*.
- 698 Spisak, N., Walczak, A.M., and Mora, T. (2020). Learning the heterogeneous hypermutation  
699 landscape of immunoglobulins from high-throughput repertoire data. *Nucleic Acids Res* *48*,  
700 10702-10712.

- 701 Storb, U., Shen, H.M., and Nicolae, D. (2009). Somatic hypermutation: processivity of the cytosine  
702 deaminase AID and error-free repair of the resulting uracils. *Cell Cycle* *8*, 3097-3101.
- 703 Sundararajan, M., Taly, A., and Yan, Q. (2017). Axiomatic Attribution for Deep Networks. ArXiv  
704 *abs/1703.01365*.
- 705 Tang, C., Bagnara, D., Chiorazzi, N., Scharff, M.D., and MacCarthy, T. (2020). AID Overlapping  
706 and Poleta Hotspots Are Key Features of Evolutionary Variation Within the Human Antibody  
707 Heavy Chain (IGHV) Genes. *Front Immunol* *11*, 788.
- 708 Tang, C., and MacCarthy, T. (2021). Characterization of DNA G-Quadruplex Structures in Human  
709 Immunoglobulin Heavy Variable (IGHV) Genes. *Frontiers in Immunology* *12*.
- 710 Wei, L., Chahwan, R., Wang, S., Wang, X., Pham, P.T., Goodman, M.F., Bergman, A., Scharff,  
711 M.D., and MacCarthy, T. (2015). Overlapping hotspots in CDRs are critical sites for V region  
712 diversification. *Proc Natl Acad Sci U S A* *112*, E728-737.
- 713 Yaari, G., Vander Heiden, J.A., Uduman, M., Gadala-Maria, D., Gupta, N., Stern, J.N., O'Connor,  
714 K.C., Hafler, D.A., Laserson, U., Vigneault, F., *et al.* (2013). Models of somatic hypermutation  
715 targeting and substitution based on synonymous mutations from high-throughput immunoglobulin  
716 sequencing data. *Front Immunol* *4*, 358.
- 717 Yu, K., Huang, F.T., and Lieber, M.R. (2004). DNA substrate length and surrounding sequence  
718 affect the activation-induced deaminase activity at cytidine. *J Biol Chem* *279*, 6496-6500.
- 719 Zhang, Z.Z., Pannunzio, N.R., Hsieh, C.L., Yu, K., and Lieber, M.R. (2014). The role of G-density  
720 in switch region repeats for immunoglobulin class switch recombination. *Nucleic Acids Res* *42*,  
721 13186-13193.
- 722 Zhou, J., and Troyanskaya, O.G. (2015). Predicting effects of noncoding variants with deep  
723 learning-based sequence model. *Nat Methods* *12*, 931-934.
- 724 Zhou, J.Q., and Kleinstein, S.H. (2020). Position-Dependent Differential Targeting of Somatic  
725 Hypermutation. *The Journal of Immunology*, *ji2000496*.  
726
- 727

728 **STAR Methods**

729

730 **Resource availability**

731

732 **Lead contact**

733 Further information and requests for resources and reagents should be directed to and will be  
734 fulfilled by the lead contact, Thomas MacCarthy ([thomas.maccarthy@stonybrook.edu](mailto:thomas.maccarthy@stonybrook.edu)).

735 **Materials availability**

736 This study did not generate new unique reagents.

737 **Data and code availability**

738 Data used for this research was published previously by Tang et al, 2020. A custom Python  
739 package developed for this project is available at <https://gitlab.com/maccarthylab/deepshm>.

740

741 **Methods details**

742

743 **Generating *k*-mer data**

744 Germline IGHV reference sequences were downloaded from the international  
745 ImMunoGeneTics information system (IMGT) website (Lefranc, 2001). The leader portion of each  
746 reference sequence was also extracted if available. To generate the  $k$ -mers of a given germline  
747 sequence,  $\pm \lfloor k/2 \rfloor$  nt sequences were extracted from the start of the V exon, where  $k$  is the length of  
748 the subsequence, and  $\lfloor k/2 \rfloor$  represents the greatest integer less than or equal to  $k/2$ . This process  
749 was continued, moving 1 nt at a time, until the end of the exon was reached. Next, all  $k$ -mers were  
750 converted to their respective one-hot encodings. A one-hot encoding is a transformation of a DNA  
751 sequence using a 2-D matrix containing only zeros and ones, where each row represents one of the  
752 four ordered DNA bases and each column is an individual site in the sequence. For each column,  
753 a "1" is filled in the row that matches the nucleotide of that site and a "0" in the remaining  
754 unmatched rows (**Figure 1**).

### 755 **Calculating mutation frequencies, substitution rates, and weighted substitutions of $k$ -mers**

756 Using a high-quality data set previously published by us (Tang et al., 2020), we calculated  
757 the mutation frequencies of every  $k$ -mer in a germline sequence as the number of observed  
758 mutations at each site (corresponding to a single  $k$ -mer), divided by the total number of sequences  
759 the germline IGHV allele contained. The substitution rate of each  $k$ -mer was computed as the  
760 number of times the middle nucleotide mutated from the germline nucleotide to the other four  
761 DNA bases, divided by the total number of overall mutations. Note that a zero was recorded in the  
762 instance the mutated base was the same as the germline context. Lastly, the weighted substitution  
763 of a  $k$ -mer was simply calculated as the observed mutation frequency multiplied by the substitution  
764 rate vector.

### 765 **CNN architecture and model optimization**



766 We implemented a convolutional neural network (CNN) to analyze the  $k$ -mer input data.  
767 Three separate architectures were used to predict different SHM outcomes: mutation frequency,  
768 substitution rate, and weighted substitution (see above). Although the hyperparameters that were  
769 ultimately selected varied from model-to-model, all CNNs followed the same general architecture,  
770 which consisted of one convolution layer, followed by two fully connected layers (**Figure 1**).  
771 Additional parameters, such as dropout and batch normalization, were optimized by generating  
772 100 separate models with randomly selected hyperparameters for each  $k$ -mer and corresponding  
773 model architecture we generated. The range of values for all parameters and hyperparameters that  
774 were tested for each architecture and output type are specified in **Supplementary Table 1**.

775 Next, we utilized 4-fold cross-validation to evaluate the performance of the model on  
776 unseen (test) data. In total, there are seven IGHV families (IGHV1-7), where each IGHV family  
777 consists of genes that share a high percentage of sequence similarity (Lefranc, 2001). The  $k$ -mers  
778 derived from the three largest IGHV families, IGHV1, IGHV3, and IGHV4, formed three separate  
779 groups, and the  $k$ -mers belonging to the remaining 4 smaller IGHV families constituted the final  
780 group in order to create a data set comparable in size with the other groups. Thus, we separated  
781 the data by their respective IGHV family to reduce the chances of model overfitting, since it is  
782 likely that  $k$ -mers from the same IGHV family will be similar even if they come from different  
783 genes and, therefore, bias the results if they appear in both training and test sets. In every cross-  
784 validation fold, three of the data groups were used as training set, and the fourth used as test set.  
785 We also evaluated the model performance, for each fold, by calculating the Pearson correlation(s)  
786 between the predicted mutation frequency and/or substitution rate of the test set  $k$ -mers and the  
787 equivalent output type of the empirical data. The average correlation across the 4 validation folds  
788 was reported for the model, as in **Figure 2**.

789 As an additional step, we wrote a custom, universal Python script (available at  
790 <https://gitlab.com/maccarthyslab/deepshm>) to automatically generate the CNN architecture,  
791 parameters, and hyperparameters of each model, regardless of the output specified, to ensure that  
792 all models were constructed in a consistent manner. All CNNs were generated using the built-in  
793 Keras API in Tensorflow 2.4.1 and trained on GPU processors using three Nvidia GeForce RTX  
794 2080 graphics cards.

### 795 **Inferring an S5F targeting model**

796 In order to ensure a fair comparison between S5F values and our deep learning predictions,  
797 we used the SHazaM R package (Yaari et al., 2013) to create an S5F targeting model, which  
798 provides analogous 5-mer mutability and substitution scores based on the same data set we used  
799 to train our CNN models with. We specified the S5F targeting model to count both silent and  
800 replacement mutations ("rs" parameter) since the mutation data we used was derived from non-  
801 functionally rearranged VDJ coding sequences (i.e. in the absence of selection) and with each  
802 sequence being clonally independent (Tang et al., 2020). Multiple mutations were handled  
803 specifying the "independent" parameter, which treats each mutation independently. Default values  
804 were used for all other parameters.

805

### 806 **Quantification and statistical analysis**

807

### 808 **Neural network encodings analysis**

809           The output (encoding) of the penultimate layer of the CNN model was used as a way to  
810 explain the SHM patterns learned by the model. To generate the encodings from this layer, we  
811 removed the last layer of the CNN while keeping the remaining layers intact. Next, we processed  
812 the  $k$ -mers through the truncated model to retrieve the ensuing output values. We then applied t-  
813 distributed stochastic neighbor embedding (t-SNE) in Python on these multidimensional encodings  
814 to visually represent the resulting embedding in two dimensions.

### 815   **Cluster identification**

816           We implemented k-means clustering to identify clusters within the t-SNE embedding of  
817 the weighted substitution model (**Supplementary Figure 1**). We separated all  $k$ -mers sharing the  
818 same middle nucleotide and then applied k-means clustering independently on each group to  
819 facilitate the clustering process. All clustering assignments were performed using the *kmeans*  
820 function in R. For each middle nucleotide, we specified the algorithm to identify 5 distinct clusters  
821 and subsequently inspected the clusters to ensure a proper separation between clusters of distinct  
822 mutabilities occurred. In the case of G and T nucleotides, there were resulting clusters (one for  
823 each nucleotide) containing hot and cold sequences (i.e one “cold” and one “hot” subcluster per  
824 cluster), so we manually split each of these clusters into two distinct (“cold” and “hot”) clusters to  
825 reduce the disparity in mutation frequencies.

### 826   **Identifying recurring genomic patterns using TF-MoDISco**

827           We applied TF-MoDISco (Shrikumar et al., 2018), a machine learning interpretability  
828 method, to identify recurring motifs our model detected in the 15-mer data. From the data, we  
829 isolated four groups of 15-mers based on the middle nucleotide (A, C, G, or T) of the 15-mer, with  
830 the additional condition that the middle nucleotide conformed to WRC or GYW AID hotspots, or

831 WA or TW Pol $\eta$  hotspots, respectively. TF-MoDISco requires importance scores to be used as  
832 input, which can be generated by utilizing one of several attribution methods. Here we generated  
833 the importance scores for each group by applying Integrated Gradients (Sundararajan et al., 2017)  
834 to the most accurate 15-mer mutation frequency model. Using the resulting importance scores, we  
835 then ran TF-MoDISco for all groups separately, still subject to the hotspot constraint, and requiring  
836 each of the identified patterns to be associated with at least 20 input sub-sequences (or “sequelents”).

837

### 838 **Key resources table**

839

REAGENT or RESOURCE	SOURCE	IDENTIFIER
Deposited data		
Data from the memory, marginal zone, and plasma cell subsets (B10-B14, B16-21, HD001-10)	Tang et al., 2020	NCBI SRA BioProject IDs 381394, 591804
Software and algorithms		
DeepSHM	This paper	<a href="https://gitlab.com/maccarthyslab/deepshm">https://gitlab.com/maccarthyslab/deepshm</a>
TF-MoDISco	Shrikumar et al., 2018	<a href="https://github.com/undajelab/tfmodisco">https://github.com/undajelab/tfmodisco</a>
SHazaM	Yaari et al., 2013	<a href="https://shazam.readthedocs.io/en/stable/">https://shazam.readthedocs.io/en/stable/</a>

840